



Gyral net: A new representation of cortical folding organization



Hanbo Chen^a, Yujie Li^a, Fangfei Ge^a, Gang Li^b, Dinggang Shen^{b,c}, Tianming Liu^{a,*}

^a Cortical Architecture Imaging and Discovery Lab, Department of Computer Science and Bioimaging Research Center, The University of Georgia, Athens, GA, USA

^b Department of Radiology and BRIC, University of North Carolina at Chapel Hill, NC, USA

^c Department of Brain and Cognitive Engineering, Korea University, Seoul 02841, Republic of Korea

ARTICLE INFO

Article history:

Received 5 January 2017

Revised 9 June 2017

Accepted 14 July 2017

Available online 15 July 2017

Keywords:

Gyral net

Cortical folding

MRI

Autism

ABSTRACT

One distinct feature of the cerebral cortex is its convex (gyri) and concave (sulci) folding patterns. Due to the remarkable complexity and variability of gyral/sulcal shapes, it has been challenging to quantitatively model their organization patterns. Inspired by the observation that the lines of gyral crests can form a connected graph on each brain hemisphere, we propose a new representation of cortical gyri/sulci organization pattern – gyral net, which models cortical architecture from a graph perspective, starting with nodes and edges obtained from the reconstructed cortical surfaces. A novel computational framework is developed to efficiently and automatically construct gyral nets from surface meshes, and four measurements are devised to quantify the folding patterns. Using an MRI dataset for autism study as a test bed, we identified reduced local connectivity cost and increased curviness of gyral net bilaterally on the parietal lobe, occipital lobe, and temporal lobe in autistic patients. Additionally, we found that the cortical thickness and the gyral straightness of gyral joints are higher than the rest of gyral crest regions. The proposed representation offers a new tool for a comprehensive and reliable characterization of the cortical folding organization. This novel computational framework will enable large-scale analyses of cortical folding patterns in the future.

© 2017 Elsevier B.V. All rights reserved.

1. Introduction

Modern magnetic resonance imaging (MRI) techniques enable *in vivo* studies of the cortical folding patterns, which attract growing research interest. It has been shown that an understanding of the cortical folding can benefit cytoarchitectonic areal parcellation (Fischl et al., 2008), normal maturation and neurodegenerative process investigation (Giedd et al., 1999), and abnormal brain development understanding (Schaer et al., 2008). As a convoluted surface, the neocortex is usually represented by a reconstructed mesh surface, upon which quantitative analyses are performed. The widely used folding pattern descriptors in the literature can be classified into two groups – global and local descriptors (Li et al., 2010). Global measurements such as surface area (Chen et al., 2012), gyration index (Zilles et al., 1988), and spherical wavelets (Yeo et al., 2008) quantify the cortical convolution level of the whole brain or preselected regions of interest (ROIs). In contrast, local descriptors, such as surface curvature, estimate the cortical folding pattern vertex-wise in a small area. Some recent works also extend

the global descriptors, such as gyration index to local scales (Li et al., 2014; Luders et al., 2006; Toro et al., 2008).

In addition to global or local analysis of cortical surfaces, another trend of studies proposed to analyze cortical folding patterns using line representations. In these studies, the skeletons of sulcal fundi and gyral crests were extracted and analyzed. Since sulcal fundi were shown more consistent across individuals (Lohmann et al., 2008), they attracted more research attention than gyral crests. For instance, different computational methods have been proposed to segment the sulcal fundi and extract skeleton lines (Kao et al., 2007; Li et al., 2009; Li and Shen, 2011; Lohmann, 1998; Lyu et al., 2010; Seong et al., 2010; Yonggang Shi et al., 2009). The shape of the extracted sulcal fundi was then quantitatively modeled (Caunce and Taylor, 2001; Tao et al., 2001) and compared across individuals and populations (Im et al., 2013; Lohmann et al., 1999). Sulcal fundi were also applied as references to register brains (Perrot et al., 2011) or segment cortical surfaces (Lohmann and von Cramon, 2000). Moreover, since the deepest sulcal regions (sulcal pits) were considered as the first cortical folds under development and that they were closely related to functional areas (Lohmann et al., 2008), further analysis on sulcal fundi have been conducted as well (Auzias et al., 2015; Im et al., 2011, 2010; Meng et al., 2014).

* Corresponding authors.

E-mail addresses: tliu@cs.uga.edu, tianming.liu@gmail.com (T. Liu).

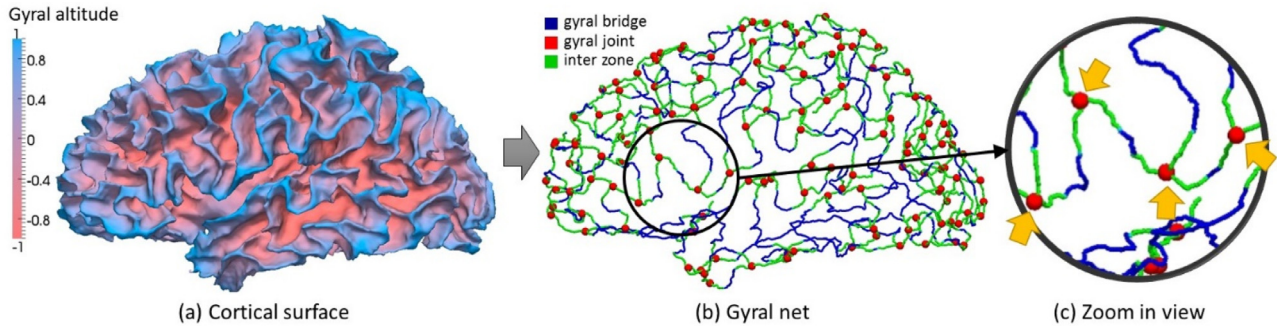


Fig. 1. Illustration of the concept of gyral net and gyral joint. (a) Reconstructed cortical surface color-coded by gyral altitude. (b) Extracted gyral net. Gyral joints, gyral bridges, and the inter zone were colored differently for illustration. (c) Zoom in view of the circled area in (b). (For interpretation of the references to color in this figure legend, the reader is referred to the web version of this article.)

In comparison, as the counterpart of sulci fundi, the morphology of gyral crest has not been thoroughly investigated. For instance, one identical feature of the gyral crest is that they form a joint when different gyri meet – namely gyral joint. However, its distribution, folding pattern, functional role, and developmental mechanism are rarely explored so far. Notably, the gyral folding pattern also plays a critical role in studying brain function and anatomy. In previous studies, gyral based regions of interest (ROIs) were shown to be biologically valid and reliable to parcellate cortical surface areas (Desikan et al., 2006). Gyral features have also been widely applied to quantify brain development (Gogtay et al., 2004) and model brain diseases (Narr et al., 2004; Nordahl et al., 2007). Further investigations on gyral folding patterns are of fundamental importance to understand brain organization.

Our previous works attempted to fill this underexplored area from different perspectives. For instance, we proposed a surface feature profiling scheme to quantify gyral folding patterns (Li et al., 2010). A quantitative examination of gyral folding patterns across primate species showed that the gyral complexity successively expressed from macaque brain to human brain (Chen et al., 2013; Li et al., 2016). We also found different connectivity patterns (Nie et al., 2012; Zhang et al., 2014) and functional roles (Deng et al., 2013; Jiang et al., 2016) between gyri and sulci. In addition, new computational models were proposed to study the mechanisms that regulate gyral development by simulating the process (Nie et al., 2010; Zhang et al., 2016). However, most of these studies only focused on specific brain ROIs. A whole-brain global representation of gyral morphology is still missing, which motivates this work.

In the early work by Lohmann (1998), a line representation of gyral crests has been proposed and extracted from 3D brain image volumes. Later on, Shi and his colleagues proposed a framework to extract gyral skeleton on the mesh surface and represent gyral crests as a graph (Shi et al., 2008). In our view, such line and graph representation of gyral crests could be a powerful abstract description of gyral morphology. However, no quantitative analysis of the extracted gyral crest lines and their joints has been conducted so far. Thus, in this work, we proposed to quantify cortical folding organizations by a graph representation – gyral net, as illustrated in Fig. 1. Specifically, we developed a new computational framework that can automatically construct the gyral net. Different from previous works, we devised a set of measures that can quantify the complexity of neocortex gyration and the local connectivity between gyri. In addition, we differentiated gyral crests by the degree of gyral net and the vertices with degree higher than two were defined as gyral joints (highlighted by yellow arrows in Fig. 1(c)). The gyral joints were extracted based on gyral net and their properties were also examined in this work. We will show that representing the cortical folding pattern by gyral net offers a more comprehensive

view such that its shape pattern, complexity, connectivity, and convolution level can be measured both locally and globally within a unified framework.

2. Method

In this paper, we extract the gyral net from the white matter cortical surface. The first step is data preprocessing and cortical surface reconstruction (Fig. 2(a) and (b), Section 2.1). Then we segmented the gyral crest area on the cortical surface (Fig. 2(c), Section 2.2). After that, the gyral net was constructed by extracting the skeletons of the gyral crests (Fig. 2(d)–(g), Section 2.3). Finally, different measurements were computed on the gyral net (Section 2.4). The method section is organized following these steps accordingly.

2.1. Data preprocessing

Data preprocessing was performed using FMRIB Software Library (FSL) (Jenkinson et al., 2012) and FreeSurfer (Fischl, 2012). In brief, we firstly resampled the 3D T1w images into 1 mm isotropic images using spline interpolation. Then, skull removal, gray matter (GM)/white matter (WM) tissue segmentation, and WM surface reconstruction were performed. During surface reconstruction, the interface between GM and WM was modeled as a triangle mesh in 3D space (Fig. 2(b)). Once the cortical surface models were complete, the gyral altitude and cortical thickness were calculated for each vertex on the reconstructed surface. Specifically, gyral altitude was defined as the dot product of the movement vector during inflation with the surface normal which can be viewed as the altitude from the current vertex to the “mid-surface” that existed between the gyri and sulci (Fig. 3(a)) (Fischl et al., 1999). Cortical thickness was calculated as the closest distance from the GM/WM boundary to the GM/CSF boundary at each vertex (Fischl and Dale, 2000). Since the surface reconstruction was performed for left hemisphere and right hemisphere separately and part of the reconstructed surfaces belongs to the cutting plane between two hemispheres, we eliminate this region with zero cortical thickness to exclude it in our analysis (Fig. 2(b)).

2.2. Gyral crest segmentation

After reconstructing the cortical surface, the next step is to segment the gyral crests on the cortical surface. Intuitively, all gyral crest areas are high in altitude. However, some gyral crests could be so deep that they fall below the “mid-surface” (Fig. 3). We adopt the watershed algorithm (Bertrand, 2005) to extract all gyral crests. In practice, an initial water level is set and the areas with their gyral altitudes lower than the water level are flooded. Each

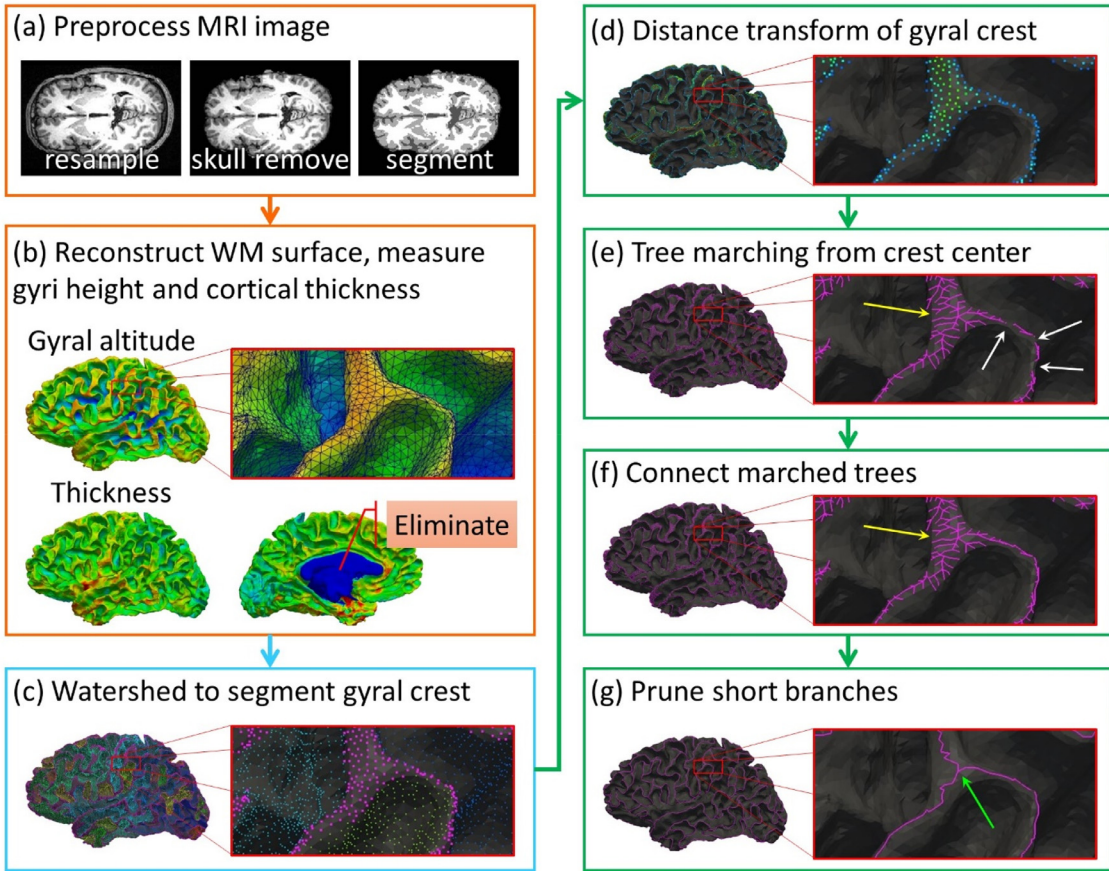


Fig. 2. The computational pipeline of our proposed method. (a) Preprocess T1-weighted MR image, including resampling image to 1 mm isotropic, skull removal, and tissue segmentation. (b) Reconstruct white matter (WM) surface as a smoothed mesh surface. An example is color-coded by gyral altitude and cortical thickness accordingly with red indicating high values and blue indicating low values. (c) Segment gyral crests using adapted watershed algorithm. Vertices on the gyral crests are shown in magenta dots and the rest vertices are colored by water sources. (d) Distance transform of the gyral crests. Gyral crest vertices are color-coded by their distance to the border. (e) Tree marching from gyral crest centers. Connections between vertices generated by marching are shown in magenta lines. (f) Connect marched trees at the gap highlighted by white arrows in (e) to form a graph. (g) Prune redundant side branches highlighted by yellow arrows in (e)–(f). (For interpretation of the references to color in this figure legend, the reader is referred to the web version of this article.)

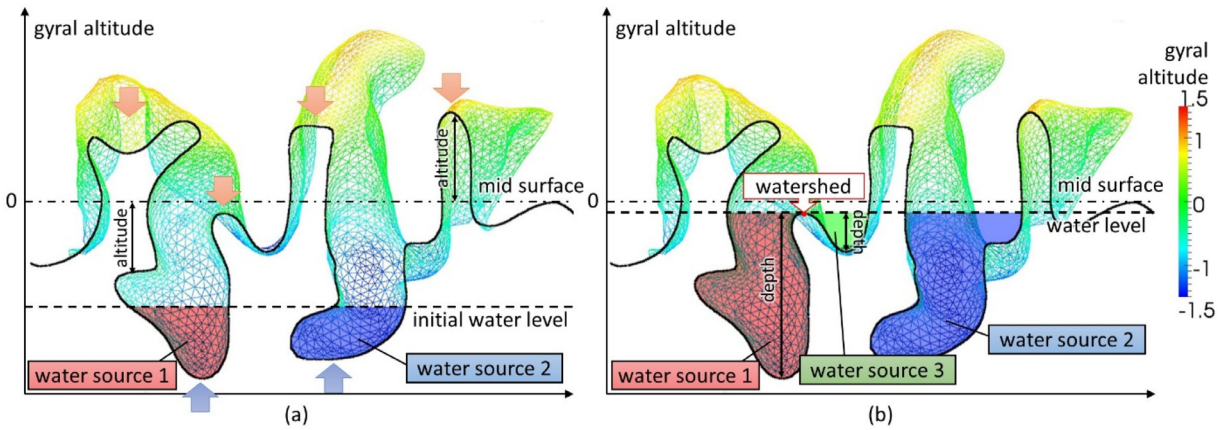


Fig. 3. Illustration of gyral crest segmentation using an adapted watershed algorithm. A piece of cortical surface mesh color-coded by gyral altitude (color bar on the right) and its cross section (black curve) are shown. Gyral crests and sulcal fundi are highlighted by red and blue arrows accordingly. (a) Initial water level. (b) Watershed emerges between two water sources after flooding. (For interpretation of the references to color in this figure legend, the reader is referred to the web version of this article.)

connected flooded area is defined as a water source (Fig. 3(a)). With the successively increased water level, each water source is growing in size. When different water sources meet, they are either merged or watersheds are built. Merging is only considered when one water source is very shallow – the depth (altitude difference between barrier peak and water source bottom, Fig. 3(b))

is smaller than a set threshold. The flooding process stops when the upper bound of water level is reached. The remaining areas above the water level together with the barriers are taken as gyral crests.

A reasonable water level threshold will help avoid false positives and false negatives in gyral crest segmentation. For instance,

Algorithm 1 Distance transform.

Input: Mesh surface $G = (\mathbf{V}, \mathbf{E})$ where \mathbf{V} is set of vertices and \mathbf{E} is set of edges, and the label of gyral crest $C \subset (0, 1)^{|\mathbf{V}|}$ such that $C_i = 1$ if and only if vertex i belongs to gyral crest.

Output: Distance transform $\mathbf{D} \subset \mathbb{R}^{|\mathbf{V}|}$ of all vertices.

1. Initialize \mathbf{D} such that $D_i = \text{Inf}$ if $C_i = 1$, otherwise $D_i = 0$
2. **While** there exist i that $D_i = \text{Inf}$
3. $\mathbf{D}^* = \mathbf{D}$
4. **For each** i that $D_i^* = \text{Inf}$
5. **If** there exist $V_j \in \text{neighbor}(V_i)$ that $D_j^* = 0$
6. $D_i = \sum_{j \in \text{neighbor}(V_i), D_j^* \neq 0} 1 / |\text{neighbor}(V_i)|$
7. **Else if** there exist $V_j \in \text{neighbor}(V_i)$ that $D_j^* \neq \text{Inf}$
8. $D_i = 1 + \sum_{j \in \text{neighbor}(V_i), D_j^* \neq \text{Inf}} D_j^* / \sum_{j \in \text{neighbor}(V_i), D_j^* \neq \text{Inf}} 1$

if the initial water level is set too low, a small convex region in a deep sulcus is also likely to be extracted as a gyral crest. On the other hand, if the final water level is set too high, some gyral crests could be missed. In addition, a reasonable merging criteria can help avoid extracting gyral crests of small concaves, which are false positives. Based on visual inspections, we empirically selected -0.7 as the initial water level, 0.7 as the final water level, and 0.3 as depth difference threshold for water source merging criteria.

2.3. Skeletons of gyral crests and gyral net

With the gyral net, we aim to represent gyral crests by lines. Ideally, the lines should follow the centers of gyral crests, which can be obtained by extracting the skeletons of gyral crest area. Inspired by the all-path-pruning algorithm (Xiao and Peng, 2013) designed for reconstructing a digital representation of neuron morphology from 2D/3D microscopy image, we proposed a novel computational framework (Fig. 2(d)–(g)) to extract the skeletons of the gyral crests on the cortical surface via the following steps.

2.3.1. Step 1: distance transform

The distance transform is firstly performed to highlight the centers of the gyral crests and generate a field with decreasing gradient from crest centers to boundaries. The classic distance-transform algorithm is defined on 2D/3D image and measures the length of the shortest path from each pixel to the border. In our approach, we extend the algorithm to measure mesh surface. The algorithm starts by setting the distance value of none-crest area to 0. Then, we will march from the borders to the centers and calculate distance value for each vertex. Since each vertex may not be connected by the same number of edges, to generate a smooth map, we modified the distance-transform algorithm and use different methods to calculate distance value for border and non-border vertices. For a border vertex, to give more weight to the vertex with more connections to the crest area, its distance is defined as the percentage of gyral crest vertex among its neighbors. For the rest vertices, their distances are calculated by adding 1 to the average distance of previously marched vertices in its neighbors. The algorithm is detailed as following: (Algorithm 1)

2.3.2. Step 2: tree marching

After distance transform, we will connect vertices from crest centers to borders by a tree marching algorithm. At the beginning, a tree root is placed in each regional maximum. From each root, a breadth-first search will be performed to construct a tree. To ensure the newly marched connections will follow the crest skeleton, we control the marching speed by applying a distance threshold such that only the vertices with the distance above the threshold can be connected. By successively decreasing this threshold value to 0, trees grow from crest centers evenly in all directions, following the crest skeletons (Fig. 4(a)–(d)). Each crest vertex will be connected and assigned to a specific tree. The whole process can be

interpreted as marching a tree structure from gyral crest centers to borders.

2.3.3. Step 3: connect trees

The next step is to connect trees to form a graph. In previous tree marching step, we did not address the scenario when two trees meet. Considering the redundant connections and abnormal short circles in gyral nets, our strategy in handling the meeting trees is to keep a record of those connections and calculate the shortest length between each pair of vertices to connect. Connections are made provided the length is longer than a selected loop threshold. A good loop threshold will help avoid small local loops on the same gyrus, while ensuring that the gyral crests can be connected into a complete net. In practice, we empirically selected 40 steps as the default loop threshold.

2.3.4. Step 4: branch pruning

During the tree marching, we connect all the vertices in crest area and some connections are the redundant branches from the skeleton to the border. The final step is to prune these redundant branches (highlighted by yellow arrows in Fig. 2(e) and (f)) generated during tree marching. For each tip vertex (vertex with degree 1), if its path length to the nearest branch vertex (vertex with degree larger than 2) is shorter than the selected length threshold, the tip vertex, as well as the vertices along its path to the branch vertex, will be viewed as redundant and thus deleted. The length threshold should be higher than the width of the widest gyrus and smaller than the length of the shortest gyrus. In our implementation, we empirically selected 10 steps as the default length threshold. Such pruning process will be performed iteratively until no more vertex can be pruned (Fig. 4(f) and (g)). After pruning, only the edges following the gyral crest skeletons will be left (Figs. 2(g) and 4(h)), which forms the final gyral net.

2.4. Quantify gyral net

The extracted gyral net is a graph representation of the cortical gyral pattern. With this representation, we are able to quantitatively measure the morphology, topology, and connectivity of gyri. In this paper, we proposed five measurements to demonstrate effective representations of the gyral pattern.

2.4.1. Gyral joint number

In our framework, each gyrus is represented by a connected curve, denoted as a gyral bridge. As illustrated in Fig. 1, the point where three or more gyral bridges meet is defined as a gyral joint. If we view the gyral net as a graph, the gyral joint will be the hub in this graph. Thus, the number of gyral joints can partially reflect the topology of the gyral net. It has been shown that the number of gyral joints in human brain is 2.5 times more than that in chimpanzee brain and 7.8 times more than that in macaque brain (Li et al., 2016). Based on this observation, it has been hypothesized that the number of gyral joints partially reflects the level of complexity of cortical folding patterns. In practice, we picked all the vertices with degree higher than 2 in gyral net and took those as gyral joints.

2.4.2. Gyral crest length

Intuitively, we can accumulate the total length of the gyral net. This metric quantifies the global size of gyral net. It is impacted by the size of brain volume, curviness of gyral crest, and total surface area, and thus it reflects the complexity of brain gyration. It also provides a simple and straight forward metric to evaluate the performance of our proposed gyral net extraction framework – the extraction is likely to be wrong when the total length is too small or too large.

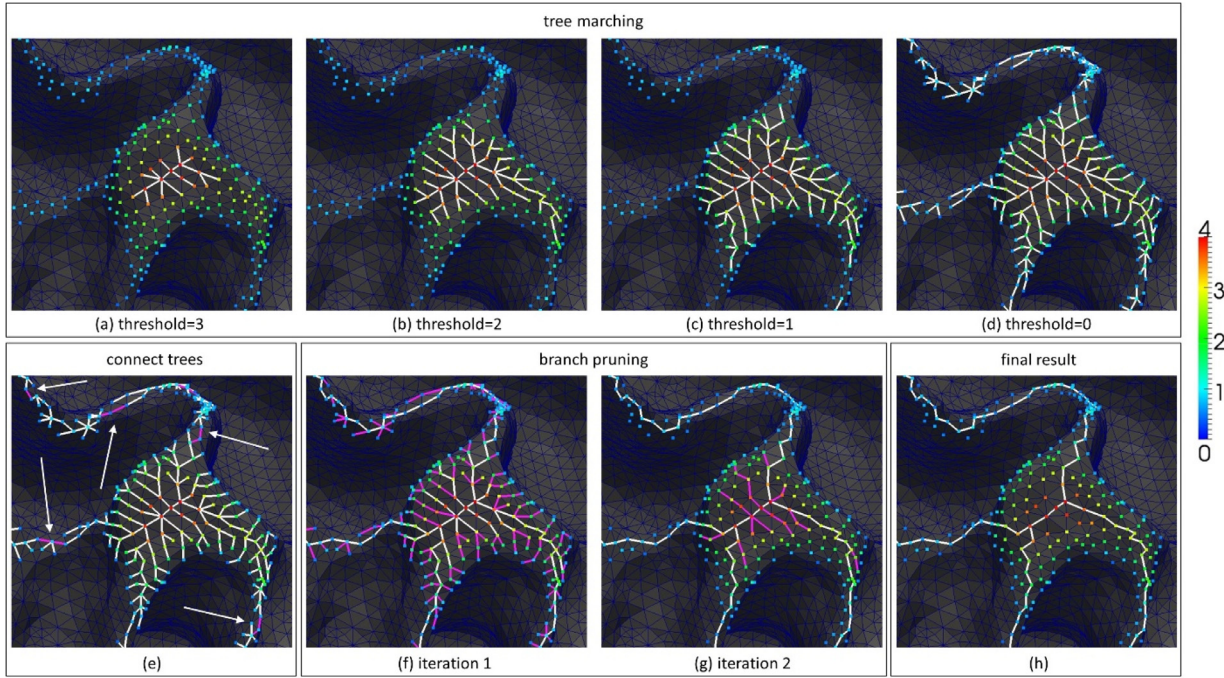


Fig. 4. Illustration of skeleton extraction of gyral crests using tree marching. Vertices on the gyral crests are shown in dots color-coded by distance transform (color bar on the right). Connections between vertices are shown in white or magenta lines. (a)–(d) Tree marching. (e) Connect trees. Connections between trees are highlighted by magenta lines and arrows. (f)–(g) Branch pruning. Pruned connections are highlighted by magenta lines. (h) Finally extracted crest skeletons. (For interpretation of the references to color in this figure legend, the reader is referred to the web version of this article.)

2.4.3. Gyral net integrity

In our observation, most gyral crests are continuously connected. Though the biological philosophy behind this phenomenon is still unclear, to quantitatively verify such a phenomenon, we proposed an integrity measurement of the gyral net. Specifically, since the gyral net is defined as vertices connected by edges, the directly or indirectly connected vertices can be grouped together into a connected component. The integrity of a gyral net is defined as the number of vertices in the largest connected component over the total number of vertices. If all the vertices on gyral crest forms a single connected component, the integrity will be 1. This measurement can serve as another global metric to verify the performance of gyral net extraction framework.

2.4.4. Local connectivity cost (LCC)

It has been shown that the surface geodesic distance between two vertices measures the intrinsic connectivity cost between them (Khan et al., 2013). In the context of gyral crest vertices, the surface geodesic distance not only reflects the spatial cost to make functional connections for intrinsic grey matter connections but also reflects the cost of extrinsic white matter connection. For this reason, the geodesic distance provides a reasonable estimate on the connectivity cost between a neuron at gyral crest with other neurons in its neighborhood. As shown in Fig. 5, the surface distance between gyral points A and B is the shortest path between them to make connections no matter it is extrinsic white matter connection or intrinsic grey matter connection. While for sulcal points D and E, the travel distance for axons to make extrinsic connections between them is much shorter than the surface distance between them.

Specifically, to measure LCC of each vertex v on the gyral net, all the surface vertices within Euclidean distance r^E are extracted. Both the surface geodesic distance and the Euclidean distance between v and its surrounding vertices are calculated. Then the averaged ratio between the surface distance and the Euclidean distance

is defined as LCC:

$$LCC(v) = \frac{1}{|W|} \sum_{w \in W} SGD(v, w) / DIST(v, w) \quad (1)$$

where $SGD(v, w)$ is the surface geodesic distance between vertices, $DIST(v, w)$ is the Euclidean distance between vertices, W is the set of surrounding vertices within radius r^E such that $W \subset V$ and $\forall w \in W, DIST(v, w) < r^E$. LCC quantifies the distance cost to make both intrinsic and extrinsic connection between a neuron on gyrus and all the other neurons close to it. A higher LCC indicates a higher cost to establish local functional connectivity and vice versa. Notably, LCC is impacted by the selection of r^E . In practice, different radii should be considered and compared.

2.4.5. Gyral crest straightness

In our previous work, we found that the gyral convolutional patterns in parallel to the cortical surface varied between primate species and could be taken as a complementary metric of brain development (Chen et al., 2014). The curvature of gyral crest line was applied to quantify such patterns. However, the curvature is not feasible when gyral crest forks into the gyral joint. Thus in this study, we proposed a new measurement – straightness, to quantify the convolutional patterns of the gyral crest. Given a vertex v on the gyral net, we found the vertex w that has the farthest Euclidean distance to v among the neighbor vertices of v along the gyral net within distance r^C . We then compare the Euclidean distance and the geodesic distance along the crest line between them such that:

$$\text{Straightness}(v) = \frac{DIST(v, w)}{CrestD(v, w)} \quad (2)$$

where $CrestD(v, w)$ is the geodesic distance between the vertices along the crest line. w is the farthest vertices to v within v 's neighborhood such that: $w \in N(v)$ and $\forall u \in N(v), CrestD(v, w) > CrestD(v, u)$, $N(v)$ is the set of surrounding vertices within distance r^C along the gyral crest line such that $N(v) \subset V$ and $\forall w \in N(v), CrestD(v,$

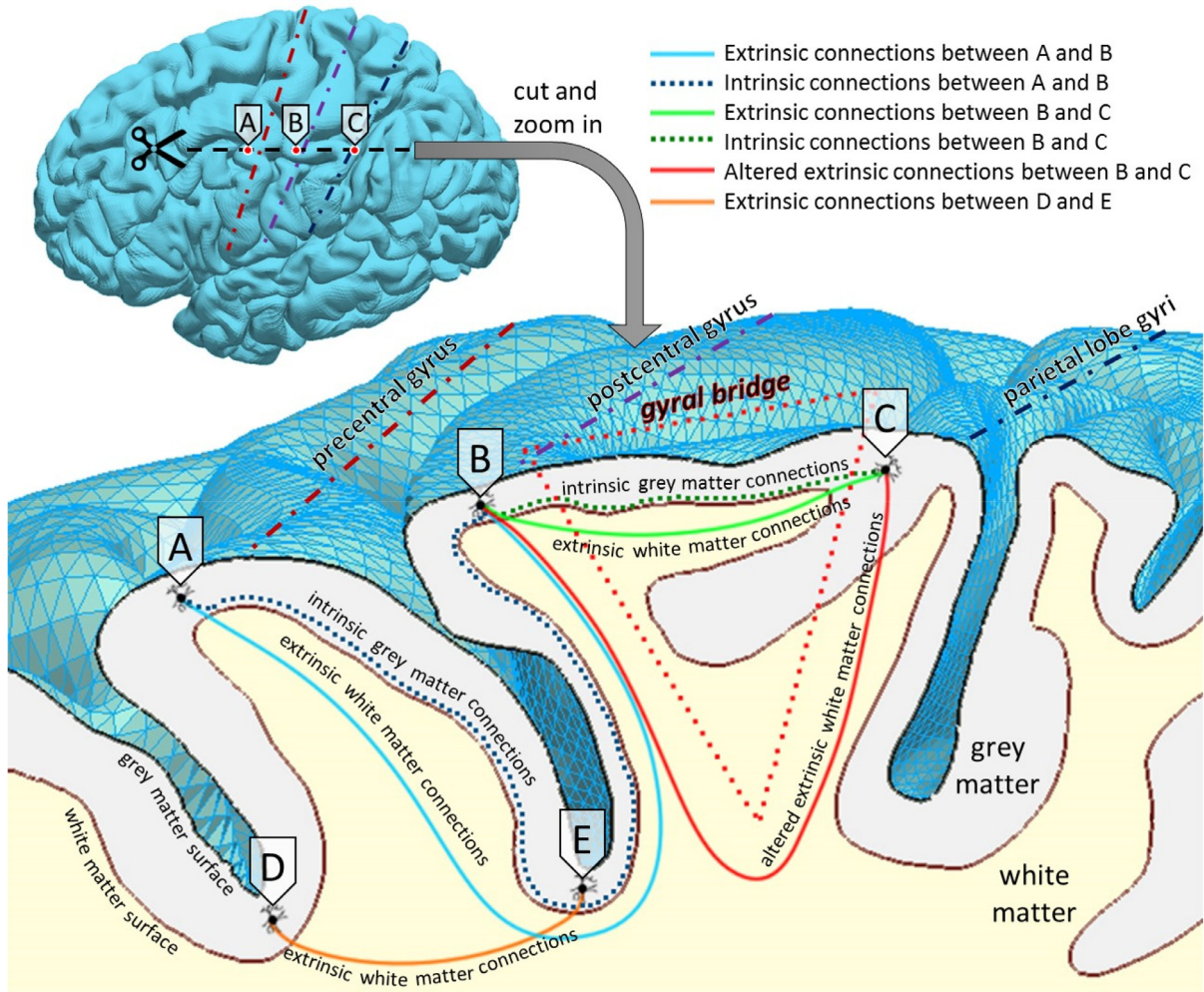


Fig. 5. Illustration of intrinsic grey matter connections (dashed curves) and extrinsic white matter connections (solid curves) in a small neighborhood. For illustration, the central gyri of a reconstructed cortical surface are dissected as shown by black dash lines. Three gyral regions (A-C) and two sulcal regions (D, E) are selected and the connections between them are shown in different colors.

$w) < r^C$. In this way, straightness can quantify the local folding pattern of gyral crests. When the gyral crest is an exactly straight line, its straightness is 1. And when the gyral crest is curved, its straightness will be relatively small.

2.5. Algorithm implementation

The gyral net extraction and quantification algorithms proposed in this paper are implemented in Matlab (<https://www.mathworks.com/>). The computational complexity for most steps such as gyral crest segmentation, distance transform, skeleton tree marching, and skeleton tree pruning is $O(|V|)$, where $|V|$ is the number of vertices that need to be processed. The most time-consuming step is the calculation of the graph distance between vertices such as the distance between adjacent tree leaves when connecting trees and the surface distance between gyral nodes when computing LCC. The computational complexity is $O(|V|^3)$. For a typical subject, the computational time required to extract and process the gyral net of one hemisphere is about 15 minutes. In the future, this can be significantly optimized by improving the distance calculation algorithm, since in our problem we do not necessarily need a precise value when the distance is larger than a threshold.

3. Applications

3.1. Experimental materials

To test the proposed framework, two different sets of data were used. First, 120 T1-weighted MRI scans acquired from 3 subjects in a test-retest experiment (Maclare et al., 2014) were applied to evaluate the reproducibility of our proposed method. The data was downloaded from <http://dx.doi.org/10.6084/m9.figshare.929651>. 40 scans were acquired for each subject in 20 separate days in a month by using a GE MR750 3T scanner. ADNI-recommended T1-weighted imaging protocol were applied and one can refer to Maclare et al. (2014) for more details.

We then analyzed the gyral net in the domain of autism spectrum disorders (ASDs). ASDs are a group of neuro-developmental conditions featured by difficulties in social interaction and communication, and repetitive patterns of behaviors, interests, or activities (Miles, 2011). Previous neuroimaging studies have shown abnormalities in both cortical anatomical folding patterns (Stigler et al., 2011) and functional connections (Khan et al., 2013; Philip et al., 2012) in ASDs.

T1 weighted MR images of ASD subjects and healthy controls (HCs), downloaded from publicly available data portal – Autism Brain Image Data Exchanged I (ABIDE I, http://fcon_1000.projects.nitrc.org/indi/abide/abide_I.html), are used in this study. Data pre-

Table 1
Description of the neuroimaging data used in this study.

Site	HC	ASD	Male	Female	Age
Total	252	185	349	88	17.3 ± 8.3
New York University Langone Medical Center	105	79	147	37	15.3 ± 6.6
Kennedy Krieger Institute	31	20	38	13	10.1 ± 1.4
Ludwig Maximilians University Munich	27	19	41	5	26.3 ± 11.4
California Institute of Technology	19	19	30	8	28.2 ± 10.6
Yale School of Medicine	18	13	22	9	13.2 ± 2.7
San Diego State University	15	3	13	5	14.8 ± 1.6
Olin Center, Institute of Living at Hartford Hospital	14	11	20	5	17.6 ± 3.3
Social Brain Lab	12	10	22	0	34.0 ± 6.9
Carnegie Mellon University	11	11	16	6	25.6 ± 4.6

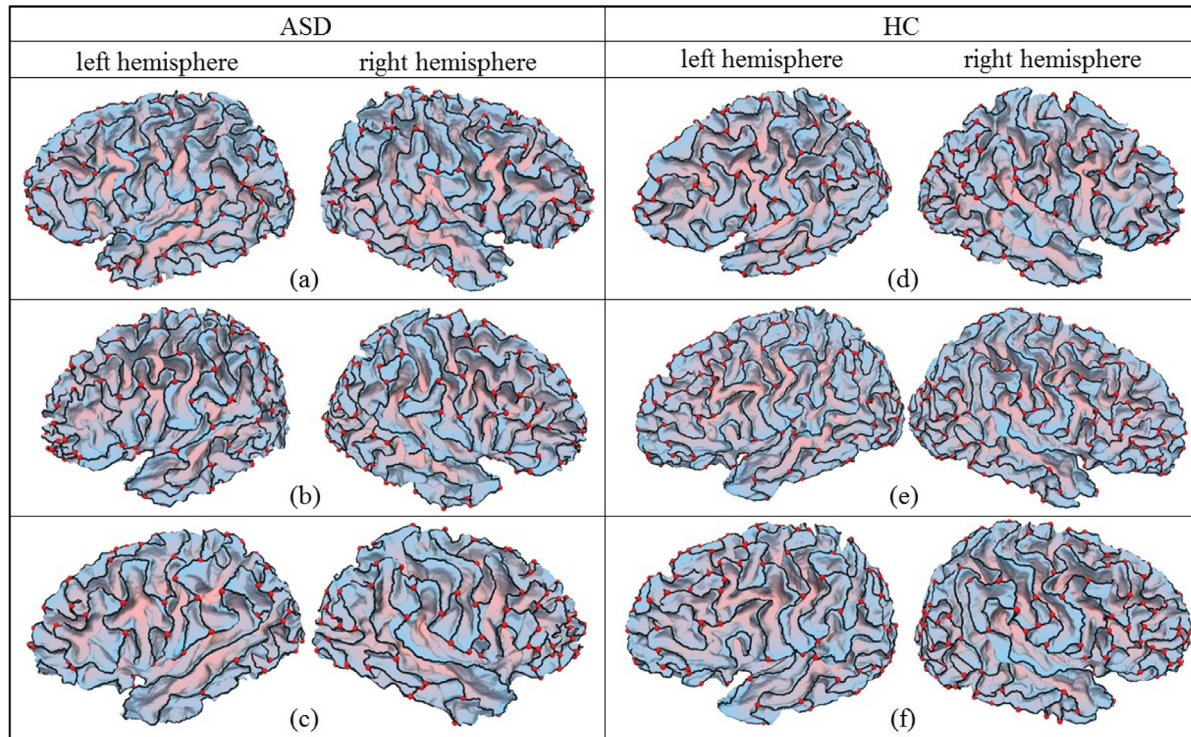


Fig. 6. Examples of extracted gyral nets (black lines) and gyral joints (red dots). Cortical surfaces are colored by gyral altitudes (pink: low, blue: high). (For interpretation of the references to color in this figure legend, the reader is referred to the web version of this article.)

processing is performed following the previous descriptions. The reconstructed cortical surfaces are then visually inspected by experts and the surfaces with obvious reconstruction errors were eliminated in our analysis. The reconstructed cortical surfaces of 437 subjects (185 ASD subjects) were finally adopted for analysis. These data were collected from 9 different sites and the related meta information was listed in Table 1. For more information, one can refer to ABIDE website.

For both datasets, we extracted and analyzed gyral net for each brain hemisphere by our proposed method. The same parameters were applied for all subjects. Examples of extracted gyral net and gyral joints were shown in Fig. 6. By visual inspection, our proposed method performed well in extracting a complete gyral net and identifying gyral joints. In our experiments, we first quantitatively evaluated the reproducibility of our proposed method. After that, we examined the properties of gyral net and gyral joints. Then we quantitatively compared the differences between healthy controls and ASD subjects.

3.2. Reproducibility experiment

By visually inspecting the results from 120 scans of 3 subjects, the morphology of extracted gyral net were shown relatively con-

sistent for each brain hemisphere of each subject. Some examples were shown in the Supplementary Fig. S1. However, it should be noted that the quality of extracted gyral nets heavily depends on the quality of reconstructed cortical surfaces. In this experiment, to verify the reproducibility of the whole pipeline, we used the same parameters for cortical surface reconstruction and accepted all the results as-is. As highlighted in Supplementary Fig. S1, when surface reconstruction varies between different scans of the same subject, the extracted gyral net also varied. Though FreeSurfer performs reasonably well on most cases, it is still critical to verify the surface reconstruction quality with visual inspection before conducting any further analysis.

To further quantitatively evaluate the reproducibility of our proposed method, for each cerebral hemisphere of each subject, we compared two global metrics (gyral net length and gyral joint number) of extracted gyral nets obtained from 40 scans. As shown in Fig. 7, both the length and the gyral joint number vary across individuals. Meanwhile, for the same hemisphere of the same subject, all the measurements followed a normal distribution among 40 scans. For gyral net length, the average standard deviation is 93.25 mm, which is 1.36% of the average gyral net length. And for gyral joint number, the average standard deviation is 5.53, which is 3.19% of the average gyral joint number.

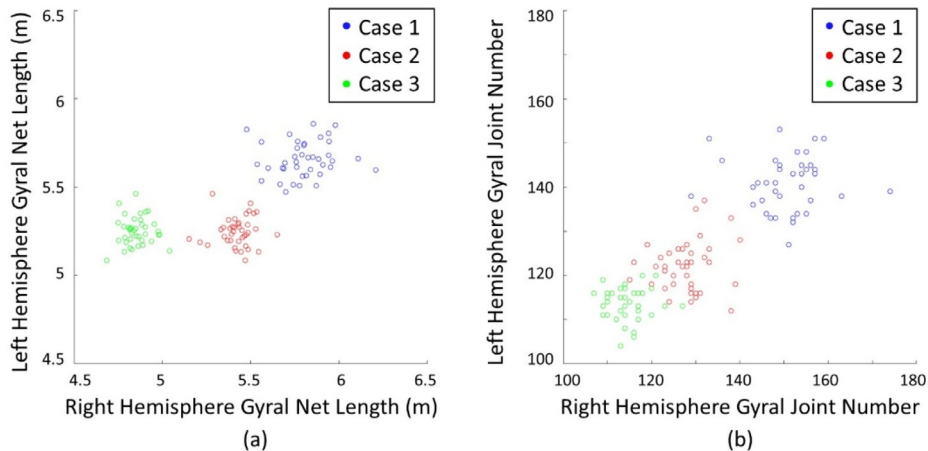


Fig. 7. Global metrics of extracted gyral nets of 120 test-retest cases. (a) Gyral net length. (b) Gyral joint number.

Table 2

Average global properties of the extracted gyral nets of all subjects including HC and ASD patients.

	HC		ASD	
	Right	Left	Right	Left
Integrity mean	0.9994	0.9993	0.9993	0.9991
Integrity minimum	0.9887	0.9875	0.9917	0.9899
Rate of integrity 1	78.57%	75.4%	76.22%	71.89%
Length mean (mm)	5639 ± 547	5618 ± 538	5704 ± 627	5659 ± 633
Gyral joint number	142.5 ± 20.5	141.9 ± 19.9	144.2 ± 22.3	141.1 ± 22.5

3.3. Global properties of gyral net

After extracting the gyral net, our first intriguing observation is that the gyral net forms a single connected component in most subjects. We use integrity to measure the completeness of the gyral net with 1 indicating a fully connected gyral net. Among all subjects, the minimum gyral net integrity is 0.9814. 79.14% of the extracted gyral nets have the integrity of 1, suggesting the reliable performance of our method. On average, the length of the gyral net is 5395.5 mm and the number of gyral joints identified on each hemisphere is 139. No significant differences are observed in these global measures between healthy controls and ASD patients ([Table 2](#)).

Another observation is that the overall length of gyral net and the total number of gyral joints are relatively symmetric between hemispheres ([Fig. 8](#)). The Pearson correlation between two hemispheres' gyral net length is 0.92. And the Pearson correlation between two hemispheres' gyral joint number is 0.81. Intriguingly, the number of gyral joint is positively correlated with the length of the gyral net ([Fig. 8\(c\)](#)). The Pearson correlation between them is 0.89. Further analyses show that both measurements are linearly correlated with the total size of white matter (WM) surface area ([Fig. 7\(d\)](#) and [\(e\)](#)). The Pearson correlation between gyral crest length and surface area is 0.93 and the Pearson correlation between gyral joint number and surface area is 0.77. By linearly rescaling the length of gyral crest length and gyral joint number of WM surface area, the correlation between those two variables drops to 0.68 ([Fig. 7\(f\)](#)). This observation suggests that the size of brain may affect the topology of cortical folding pattern.

3.4. Local measurements of gyral bridge and gyral joints

After extracting the gyral net, we identified the vertices with degree higher than 2 as gyral joints. Similar to sulcal pits, gyral

joints could potentially be taken as landmarks to establish a correspondence between brains and to quantify cortical morphology. To evaluate the properties of gyral joint, we compared the local measurements between gyral joints and the rest part of gyral net – namely, gyral bridges. Notably, the vertices within 10 mm of gyral joint were labeled as the inter zone and excluded from this analysis. The definitions of gyral joint, gyral bridge, and inter zone were illustrated in [Fig. 1](#). Notably, the inter zone is defined to clearly differentiate gyral joint and gyral bridge for comparison purpose only.

In this experiment, we included all the subjects and did not differentiate hemispheres and ASD subjects and healthy controls. Intriguingly, gyral joints are significantly thicker than gyral bridges (paired-sample *t*-test *p*-value is 0). On average, the gyral joint is 3.13 ± 0.24 mm in thickness and the gyral bridge is 2.90 ± 0.22 mm in thickness. Moreover, gyral joints are relatively flatter than gyral bridges. The average mean curvature of gyral joints (-0.26 ± 0.01) is significantly closer to 0 than gyral bridge (-0.31 ± 0.01 , paired-sample *t*-test *p*-value is 0). We then compared LCC and gyral crest straightness between gyral joints and gyral bridges. Notably, these two measurements need to define the radius of the neighborhood before computation. We empirically selected 4 different radius values (5, 10, 15, and 20 mm) to compute and the results were shown in [Table 3](#). It is interesting that the gyral nets radiated from the gyral joints are straighter than the gyral bridges. Also, the gyral joints have smaller LCC than the gyral bridges. Such differences were consistent with different radius selections and were shown significant by paired-sample *t*-test (*p*-values are close to 0). Some examples were shown in [Fig. 9](#). The possible mechanism behind this phenomenon will be discussed later.

3.5. Gyral net abnormality in ASD

No significant difference between ASD subjects and healthy controls was identified in our previous global analysis of gyral net. In this section, we will investigate the differences between local measurements of the gyral crest. Specifically, we will compare averaged gyral net measurements including LCC and straightness within each region of interest (ROI). Five brain ROIs were defined and analyzed accordingly including frontal lobe (FL), central gyri (CG), parietal and occipital lobe (POL), temporal lobe (TL), and cingulate cortex (CC).

Intriguingly, we found that the LCC in ASD subjects' brain is overall lower than healthy controls' brain. And such difference is more significant in the left parietal lobe, left occipital lobe, and left temporal lobe than other brain regions. We showed the results

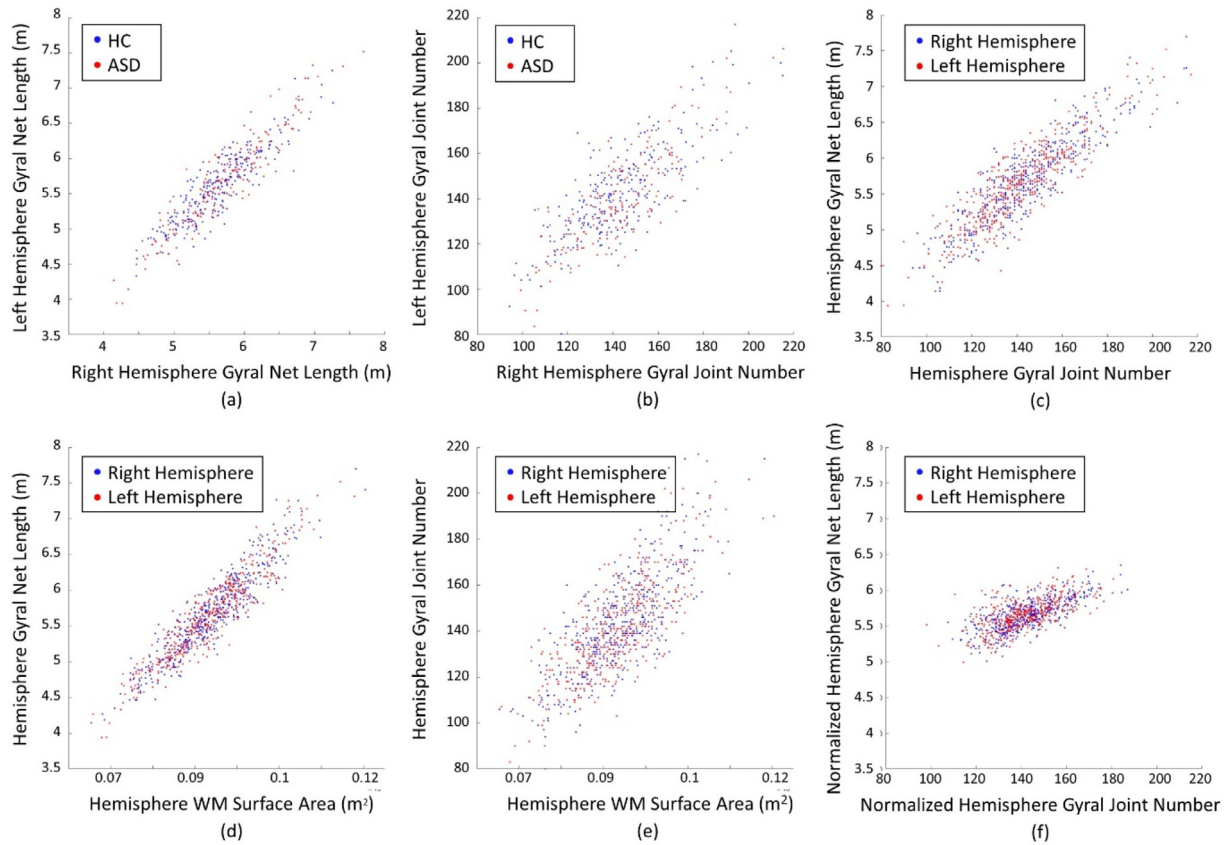


Fig. 8. Scatter plots of gyral net length and gyral joint number. In (a)–(b), each dot represents a subject. In (c)–(f), each dot represents a hemisphere. (a) Correlation between gyral net length of right and left hemispheres in different populations. (b) Correlation between gyral joint number of right and left hemispheres in different populations. (c) Correlation between the gyral joint number and gyral net length. (d) Correlation between white matter (WM) cortical surface area and gyral net length. (e) Correlation between WM surface area and gyral joint number. (f) Correlation between the gyral joint number and gyral net length normalized by WM surface area.

Table 3
Average local measurements of gyral joints and gyral bridges among all subjects with different radiuses.

Radius (mm)		5	10	15	20
LCC	Bridge	1.08 ± 0.04	1.75 ± 0.09	1.91 ± 0.07	1.92 ± 0.06
	Joint	1.07 ± 0.03	1.45 ± 0.07	1.66 ± 0.07	1.71 ± 0.06
Straightness	Bridge	0.80 ± 0.01	0.73 ± 0.02	0.69 ± 0.02	0.65 ± 0.02
	Joint	0.81 ± 0.01	0.75 ± 0.01	0.70 ± 0.01	0.66 ± 0.01
Thickness (mm)	Bridge	2.90 ± 0.22			
	Joint	3.13 ± 0.24			
Mean Curvature	Bridge	-0.31 ± 0.01			
	Joint	-0.26 ± 0.01			

when the radius is 10 mm in Table 4 and more results can be found in Supplementary Table S 1. Such finding is consistent among different radius selections.

Moreover, healthy controls' gyral nets were shown to be straighter than ASD patients' ones (Table 5). The higher straightness was also shown to be significant in the temporal lobe with different radius selections (Supplementary Table S 2). These findings coincide with the findings in previous studies that ASD patients' cerebral cortices have increased gyration than normal controls.

Since gyral crest straightness only quantified the gyral folding pattern in the tangential direction of the cortical surface, there is a possibility that the abnormal cortical folding pattern exists in the normal direction of the cortical surface. Intuitively, a deeper sulcus could result in higher LCC. Thus, we presumed that there is decreased sulcal depth in ASD patients, which result in decreased LCC. However, no significant difference in the gyral altitude be-

tween ASD patients and healthy controls was observed (Supplementary Table S7). Since this altitude did not capture the depth information of adjacent sulci, we further analyzed the height of gyrus, which is defined as the altitude difference between a gyral crest vertex and the deepest point in its neighborhood (vertices within 20 mm geodesic distance). Still, no significant difference was observed (Supplementary Table S8).

Another important metric to quantify cortical folding pattern is cortical thickness. The correlation between cortical thickness, brain development, and mental disorders have been widely studied in literature (Antonio Y. Hardan et al., 2006; Giedd and Rapoport, 2010). To test whether the abnormal cortical folding patterns we observed in ASD patients are correlated with abnormal cortical thickness, we analyzed both the average cortical thickness in the whole ROI and the average cortical thickness of gyral crests only. However, no significantly different cortical thickness between two

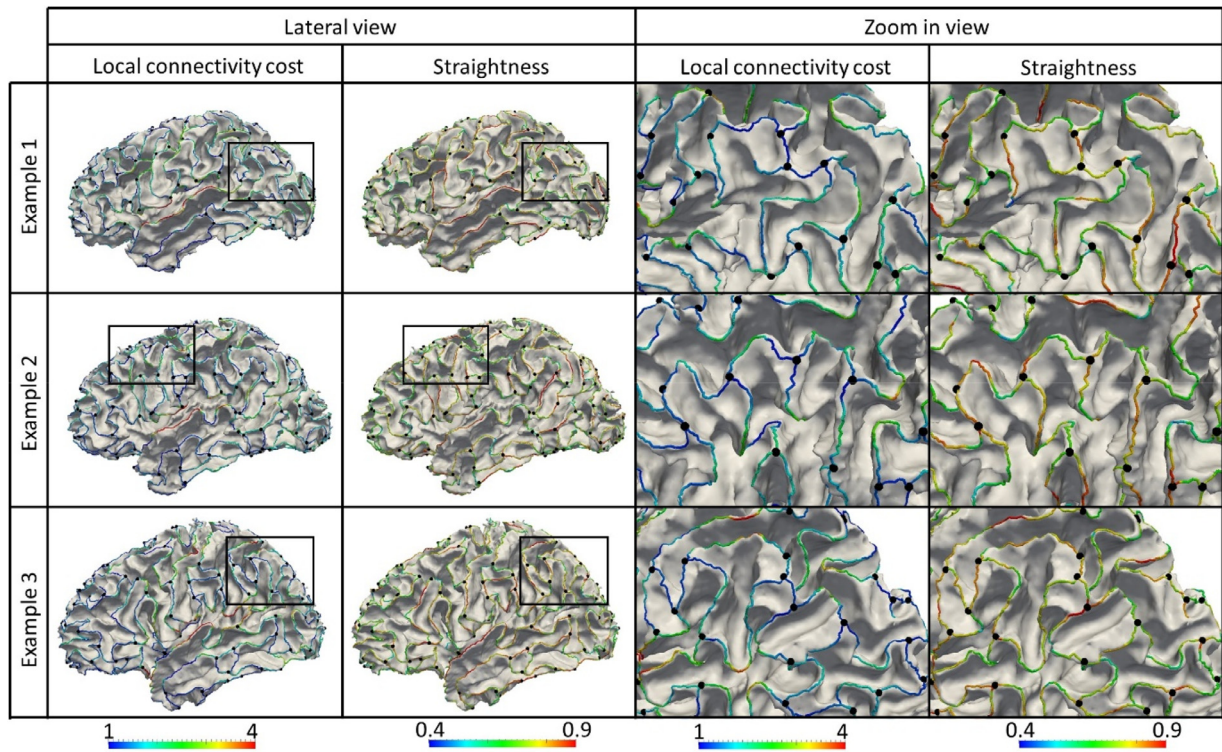


Fig. 9. Illustration of gyral nets, color coded by local connectivity cost or straightness. The color bar is at the bottom. A zoom in view of the regions highlighted by the black box is shown on the right. Identified gyral joints are highlighted by black dots. (For interpretation of the references to color in this figure legend, the reader is referred to the web version of this article.)

Table 4

Average LCC of the gyral net in different brain regions when the Euclidean radius is 10 mm. FL: frontal lobe, CG: central gyrus, POL: parietal and occipital lobe, TL: temporal lobe, CC: cingulate cortex, all: whole hemisphere. The p-value of two-sample *t*-test and the false discovery rate (FDR, exclude the measurements on whole hemisphere) (Benjamini and Hochberg, 1995) were also shown.

ROI	Right hemisphere				Left hemisphere			
	HC	ASD	p-value	FDR	HC	ASD	p-value	FDR
FL	1.452 ± 0.060	1.450 ± 0.063	7.9e-01	0.8300	1.440 ± 0.057	1.433 ± 0.058	1.7e-01	0.3400
CG	1.914 ± 0.156	1.902 ± 0.156	4.2e-01	0.6571	1.896 ± 0.157	1.888 ± 0.153	5.9e-01	0.7375
POL	1.778 ± 0.088	1.763 ± 0.090	7.6e-02	0.1900	1.781 ± 0.090	1.749 ± 0.098	4.9e-04	0.0049
TL	1.613 ± 0.104	1.593 ± 0.104	5.1e-02	0.1700	1.635 ± 0.097	1.605 ± 0.104	2.1e-03	0.0105
CC	1.360 ± 0.090	1.358 ± 0.099	8.3e-01	0.8300	1.338 ± 0.088	1.344 ± 0.095	4.6e-01	0.6571
all	1.619 ± 0.065	1.608 ± 0.068	8.0e-02	–	1.620 ± 0.067	1.601 ± 0.068	3.1e-03	–

Table 5

Average straightness of gyral net in different brain regions when the geodesic radius is 10 mm. FL: frontal lobe, CG: central gyrus, POL: parietal and occipital lobe, TL: temporal lobe, CC: cingulate cortex, all: whole hemisphere. The p-value of two-sample *t*-test and the false discovery rate (FDR, exclude the measurements on whole hemisphere) were also shown.

ROI	Right				Left			
	HC	ASD	p-value	FDR	HC	ASD	p-value	FDR
FL	0.714 ± 0.016	0.710 ± 0.017	1.9e-02	0.0633	0.718 ± 0.015	0.717 ± 0.016	3.5e-01	0.4375
CG	0.741 ± 0.020	0.740 ± 0.021	7.6e-01	0.8444	0.738 ± 0.019	0.736 ± 0.018	1.5e-01	0.2500
POL	0.728 ± 0.014	0.726 ± 0.015	9.4e-02	0.1880	0.729 ± 0.014	0.727 ± 0.015	5.8e-02	0.1450
TL	0.736 ± 0.018	0.730 ± 0.018	2.7e-03	0.0180	0.734 ± 0.019	0.728 ± 0.020	3.6e-03	0.0180
CC	0.768 ± 0.023	0.766 ± 0.022	3.5e-01	0.4375	0.770 ± 0.023	0.770 ± 0.023	9.0e-01	0.9000
all	0.729 ± 0.013	0.726 ± 0.013	1.1e-02	–	0.731 ± 0.013	0.728 ± 0.013	2.7e-02	–

populations was observed in the defined ROIs (Supplementary Tables S5, S6).

In the previous section, we showed that the gyral joint has lower LCC and higher straightness than the gyral bridge. Thus we wonder if the differences in LCC and straightness in ASD patients' brain are related to the different numbers or distributions of gyral

joints. However, as shown in Supplementary Table S9, there is no significant difference on the number of gyral joint. We also studied the distribution of gyral joint by analyzing the percentage of the gyral net that locates within the neighborhood of gyral joint. This measurement will tell us if gyral joint concentrate in a small area (low coverage) or evenly spread (high coverage). However, still, no

significant difference was found between healthy controls and ASD patients (Supplementary Table S3-S4).

If we fix both the Euclidean distance radius of LCC and the geodesic distance radius of straightness to 10 mm, 7 metrics that are significantly different between ASD patients and healthy controls were obtained as highlighted in bold in Tables 4 and 5. To further evaluate the diagnostic value of these metrics, a decision tree ensemble classifier was trained using AdaBoost (Freund and Schapire, 1995) to predict whether the MR image came from an autism patient, based on these 7 features. With 10-folds cross-validations, the classification error is 38.9%. Though the performance is not ideal, certain levels of folding pattern differences between healthy controls and ASD patients were captured by our proposed metrics.

4. Discussion and conclusion

In this work, we proposed a novel graph representation of cortical morphology – gyral net. A computational framework has been proposed to automatically extract gyral net and gyral joints. By analyzing the gyral nets of 437 subjects from ASD patients and normal subjects, we had two interesting observations in our results. 1) Gyral joints have very different properties than other gyral crest regions. 2) ASD patients' gyral nets have lower local connectivity costs and are more curved than those of healthy controls.

Intuitively, the lower local connectivity cost in the gyral joint area is largely due to the special cortical geometry in its surroundings. As illustrated in Fig. 5, when points B and C on the gyral crest are connected via a gyral bridge, the travel distance required to make connections between them is relatively low (green lines) indicating a low local connectivity cost. Simultaneously, gyral joints will be formed at point B and C. On the other hand, if we removed the gyrus between them as illustrated by red dash lines, the travel distance of the axons between B and C will significantly increase (red line) resulting in a high local connectivity cost. One interesting hypothesis behind this observation is that, with a relatively low local connectivity cost, will the functional role of gyral joints differentiate from other brain regions? Further analysis on functional imaging could answer this question.

The higher thickness and straightness in the gyral joints we observed is quite intriguing. In the previous studies, researchers have reported the difference in cortical thickness between gyral and sulcal areas (Fischl and Dale, 2000; Li et al., 2015). However, the difference in thickness between gyral joint and other gyral crest regions have been rarely investigated. This observation could offer new insight into the developmental mechanism of the cortical surface that regulates the emerging of cortical folds. In previous studies, different hypotheses of the physical mechanism that regulates the cortical landscape have been proposed, including differential cortical expansion (Bayly et al., 2014; Rash et al., 2013; Ronan et al., 2013) and neuron wiring (Nie et al., 2012; Van Essen, 1997; Xu et al., 2010). Based on the thicker cortex in gyral joints, we hypothesize that the gyral joint could be the earliest emerging area of a gyrus and there could be more axonal fibers concentrating on gyral joints than other gyral crest regions. Meanwhile, the higher straightness in gyral joints could be due to the relatively stable triangle shape in its neighborhood. However, to fully understand the mechanism behind these observations, further investigations on brain developmental data and mechanical simulations are needed.

Our findings on ASD patients' brains are consistent with the previous findings that ASD patients' brains have increased gyration (Hardan et al., 2004; Nordahl et al., 2007; Stigler et al., 2011; Wallace et al., 2013). Similar to the recent findings by Wallace and his colleagues (Wallace et al., 2013), we found increased gyral convolution in the temporal lobe, parietal lobe, and occipital lobe, al-

though the overall size of the gyral net remains the same between ASD patients and healthy controls. Instead of focusing on the cortical convolution patterns in the radial direction of the cortex (e.g., sulcal depth), our proposed straightness metric mainly quantifies the convolution patterns in the tangential direction of the cortex.

In the future works, more analyses on the gyral nets and gyral joints using different image modalities and longitudinal data are needed to fully understand their functional roles, connectivity properties, and development mechanisms. The proposed gyral net representation can be further adopted to study neurodevelopmental processes and other brain diseases. Based on the extracted gyral nets, an automatic searching framework will be developed to identify novel cortical landmarks such as the consistent gyral joints introduced in (Li et al., 2016). In addition, the state of art graph matching and deep learning algorithms (Li et al., 2017) can be developed to align gyral nets for group-wise analysis in the future.

Acknowledgements

T Liu was partially supported by National Institutes of Health (DA033393, AG042599) and National Science Foundation (IIS-1149260, CBET-1302089, BCS-1439051 and DBI-1564736). D Shen was partially supported by National Institutes of Health (EB006733, MH100217). G Li was partially supported by National Institutes of Health (MH107815, MH108914). We would like to thank the ABIDE project for sharing the datasets used in this work.

Supplementary materials

Supplementary material associated with this article can be found, in the online version, at doi:10.1016/j.media.2017.07.001.

References

- Antonio Y. Hardan, M.D., Sri Muddasani, M.D., Madhuri Vemulapalli, M.S., Matcheri S. Keshavan, M.D., Nancy J. Minshew, M.D., 2006. An MRI study of increased cortical thickness in autism. *American Journal of Psychiatry. Am. Psychiatric Assoc.*
- Auzias, G., Brun, L., Deruelle, C., Coulon, O., 2015. Deep sulcal landmarks: Algorithmic and conceptual improvements in the definition and extraction of sulcal pits. *Neuroimage* 111, 12–25. doi:10.1016/j.neuroimage.2015.02.008.
- Bayly, P.V., Taber, L.A., Kroenke, C.D., 2014. Mechanical forces in cerebral cortical folding: A review of measurements and models. *J. Mech. Behav. Biomed. Mater.* 29, 568–581. doi:10.1016/j.jmbbm.2013.02.018.
- Benjamini, Y., Hochberg, Y., 1995. Controlling the false discovery rate: a practical and powerful approach to multiple testing. *J. R. Stat. Soc. Ser. B.*
- Bertrand, G., 2005. On topological watersheds. *J. Math. Imaging Vis.* 22, 217–230. doi:10.1007/s10851-005-4891-5.
- Caunce, A., Taylor, C.J., 2001. Building 3D sulcal models using local geometry. *Med. Image Anal.* 5, 69–80. doi:10.1016/S1361-8415(00)00033-5.
- Chen, C.-H., Gutierrez, E.D., Thompson, W., Panizzon, M.S., Jernigan, T.L., Eyler, L.T., Fennema-Notestine, C., Jak, A.J., Neale, M.C., Franz, C.E., Lyons, M.J., Grant, M.D., Fischl, B., Seidman, L.J., Tsuang, M.T., Kremen, W.S., Dale, A.M., 2012. Hierarchical genetic organization of human cortical surface area. *Science* 335, 1634–1636. doi:10.1126/science.1215330.
- Chen, H., Yu, X., Jiang, X., Li, K., Li, L., Hu, X., Han, J., Guo, L., Hu, X., Liu, T., 2014. Evolutionarily-preserved consistent gyral folding patterns across primate brains. In: ISBI. IEEE, pp. 1218–1221. doi:10.1109/ISBI.2014.6868095.
- Chen, H., Zhang, T., Guo, L., Li, K., Yu, X., Li, L., Hu, X.X., Han, J., Liu, T., 2013. Co-evolution of gyral folding and structural connection patterns in primate brains. *Cereb. Cortex* 23, 1208–1217. doi:10.1093/cercor/bhs113.
- Deng, F., Jiang, X., Zhu, D., Zhang, T., Li, K., Guo, L., Liu, T., 2013. A functional model of cortical gyri and sulci. *Brain Struct. Funct.* doi:10.1007/s00429-013-0581-z.
- Desikan, R.S., Ségonne, F., Fischl, B., Quinn, B.T., Dickerson, B.C., Blacker, D., Buckner, R.L., Dale, A.M., Maguire, R.P., Hyman, B.T., Albert, M.S., Killiany, R.J., 2006. An automated labeling system for subdividing the human cerebral cortex on MRI scans into gyral based regions of interest. *Neuroimage* 31, 968–980. doi:10.1016/j.neuroimage.2006.01.021.
- Fischl, B., 2012. FreeSurfer. *Neuroimage* 62, 774–781. doi:10.1016/j.neuroimage.2012.01.021.
- Fischl, B., Dale, A.M., 2000. Measuring the thickness of the human cerebral cortex from magnetic resonance images. *Proc. Natl. Acad. Sci. U. S. A.* 97, 11050–11055. doi:10.1073/pnas.200033797.
- Fischl, B., Rajendran, N., Busa, E., Augustinack, J., Hinds, O., Yeo, B.T.T., Mohlberg, H., Amunts, K., Zilles, K., 2008. Cortical folding patterns and predicting cytoarchitecture. *Cereb. Cortex* 18, 1973–1980. doi:10.1093/cercor/bhm225.

- Fischl, B., Sereno, M.I., Dale, A.M., 1999. Cortical surface-based analysis: II: inflation, flattening, and a surface-based coordinate system. *Neuroimage* 9, 195–207.
- Freund, Y., Schapire, R.E., 1995. A Desicion-Theoretic Generalization of On-Line Learning and an Application to Boosting. Springer, pp. 23–37. doi:[10.1007/3-540-59119-2_166](https://doi.org/10.1007/3-540-59119-2_166).
- Giedd, J.N., Blumenthal, J., Jeffries, N.O., Castellanos, F.X., Liu, H., Zijdenbos, A., Paus, T., Evans, A.C., Rapoport, J.L., 1999. Brain development during childhood and adolescence: a longitudinal MRI study. *Nat. Neurosci.* 2, 861–863. doi:[10.1038/13158](https://doi.org/10.1038/13158).
- Giedd, J.N., Rapoport, J.L., 2010. Structural MRI of Pediatric brain development: what have we learned and where are we going? *Neuron* 67, 728–734. doi:[10.1016/j.neuron.2010.08.040](https://doi.org/10.1016/j.neuron.2010.08.040).
- Gogtay, N., Giedd, J.N., Lusk, L., Hayashi, K.M., Greenstein, D., Vaituzis, A.C., Nugent, T.F., Herman, D.H., Clasen, L.S., Toga, A.W., Rapoport, J.L., Thompson, P.M., 2004. Dynamic mapping of human cortical development during childhood through early adulthood. *Proc. Natl. Acad. Sci. U. S. A.* 101, 8174–8179. doi:[10.1073/pnas.0402680101](https://doi.org/10.1073/pnas.0402680101).
- Hardan, A.Y., Jou, R.J., Keshavan, M.S., Varma, R., Minshew, N.J., 2004. Increased frontal cortical folding in autism: a preliminary MRI study. *Psychiatry Res* 131, 263–268. doi:[10.1016/j.pscychresns.2004.06.001](https://doi.org/10.1016/j.pscychresns.2004.06.001).
- Im, K., Choi, Y.Y., Yang, J.-J., Lee, K.H., Kim, S.I., Grant, P.E., Lee, J.-M., 2011. The relationship between the presence of sulcal pits and intelligence in human brains. *Neuroimage* 55, 1490–1496. doi:[10.1016/j.neuroimage.2010.12.080](https://doi.org/10.1016/j.neuroimage.2010.12.080).
- Im, K., Jo, H.J., Mangin, J.-F., Evans, A.C., Kim, S.I., Lee, J.-M., 2010. Spatial distribution of deep sulcal landmarks and hemispherical asymmetry on the cortical surface. *Cereb. Cortex* 20, 602–611. doi:[10.1093/cercor/bhp127](https://doi.org/10.1093/cercor/bhp127).
- Im, K., Pienaar, R., Paldino, M.J., Gaab, N., Galaburda, A.M., Grant, P.E., 2013. Quantification and discrimination of abnormal sulcal patterns in polymicrogyria. *Cereb. Cortex* 23, 3007–3015. doi:[10.1093/cercor/bhs292](https://doi.org/10.1093/cercor/bhs292).
- Jenkinson, M., Beckmann, C.F., Behrens, T.E., Woolrich, M.W., Smith, S.M., 2012. FSL. *Neuroimage* 62, 782–790.
- Jiang, X., Li, X., Lv, J., Zhao, S., Zhang, S., Zhang, W., Zhang, T., Han, J., Guo, L., Liu, T., 2016. Temporal dynamics assessment of spatial overlap pattern of functional brain networks reveals novel functional architecture of cerebral cortex. *IEEE Trans. Biomed. Eng.* 1–1, doi:[10.1109/TBME.2016.2598728](https://doi.org/10.1109/TBME.2016.2598728).
- Kao, C.-Y., Hofer, M., Sapiro, G., Stern, J., Rehm, K., Rottenberg, D.A., 2007. A geometric method for automatic extraction of sulcal fundi. *IEEE Trans. Med. Imaging* 26, 530–540. doi:[10.1109/TMI.2006.886810](https://doi.org/10.1109/TMI.2006.886810).
- Khan, S., Gramfort, A., Shetty, N.R., Kitzbichler, M.G., Ganesan, S., Moran, J.M., Lee, S.M., Gabrieli, J.D.E., Tager-Flusberg, H.B., Joseph, R.M., Herbert, M.R., Hämäläinen, M.S., Kenet, T., 2013. Local and long-range functional connectivity is reduced in concert in autism spectrum disorders. *Proc. Natl. Acad. Sci. U. S. A.* 110, 3107–3112. doi:[10.1073/pnas.1214533110](https://doi.org/10.1073/pnas.1214533110).
- Li, G., Guo, L., Nie, J., Liu, T., 2009. Automatic cortical sulcal parcellation based on surface principal direction flow field tracking. *Neuroimage* 46, 923–937. doi:[10.1016/j.neuroimage.2009.03.039](https://doi.org/10.1016/j.neuroimage.2009.03.039).
- Li, G., Lin, W., Gilmore, J.H., Shen, D., 2015. Spatial patterns, longitudinal development, and hemispheric asymmetries of cortical thickness in infants from birth to 2 years of age. *J. Neurosci.* 35.
- Li, G., Shen, D., 2011. Consistent sulcal parcellation of longitudinal cortical surfaces. *Neuroimage* 57, 76–88. doi:[10.1016/j.neuroimage.2011.03.064](https://doi.org/10.1016/j.neuroimage.2011.03.064).
- Li, G., Wang, L., Shi, F., Lyall, A.E., Lin, W., Gilmore, J.H., Shen, D., 2014. Mapping longitudinal development of local cortical gyration in infants from birth to 2 years of age. *J. Neurosci.* 34, 4228–4238. doi:[10.1523/JNEUROSCI.3976-13.2014](https://doi.org/10.1523/JNEUROSCI.3976-13.2014).
- Li, J., Xu, K., Chaudhuri, S., Yumer, E., Zhang, H., Guibas, L., 2017. GRASS: Generative recursive autoencoders for shape structures. doi:[10.1145/3072959.3073613](https://doi.org/10.1145/3072959.3073613).
- Li, K., Guo, L., Li, G., Nie, J., Faraco, C., Cui, G., Zhao, Q., Miller, L.S., Liu, T., 2010. Gyral folding pattern analysis via surface profiling. *Neuroimage* 52, 1202–1214. doi:[10.1016/j.neuroimage.2010.04.263](https://doi.org/10.1016/j.neuroimage.2010.04.263).
- Li, X., Chen, H., Zhang, T., Yu, X., Jiang, X., Li, K., Li, L., Razavi, M.J., Wang, X., Hu, X., Han, J., Guo, L., Hu, X., Liu, T., 2016. Commonly preserved and species-specific gyral folding patterns across primate brains. *Brain Struct. Funct.* 1–15. doi:[10.1007/s00429-016-1329-3](https://doi.org/10.1007/s00429-016-1329-3).
- Lohmann, G., 1998. Extracting line representations of sulcal and gyral patterns in MR images of the human brain. *IEEE Trans. Med. Imaging* 17, 1040–1048. doi:[10.1109/42.746714](https://doi.org/10.1109/42.746714).
- Lohmann, G., von Cramon, D.Y., 2000. Automatic labelling of the human cortical surface using sulcal basins. *Med. Image Anal.* 4, 179–188. doi:[10.1016/S1361-8415\(00\)00024-4](https://doi.org/10.1016/S1361-8415(00)00024-4).
- Lohmann, G., von Cramon, D.Y., Colchester, A.C.F., 2008. Deep sulcal landmarks provide an organizing framework for human cortical folding. *Cereb. Cortex* 18, 1415–1420. doi:[10.1093/cercor/bhm174](https://doi.org/10.1093/cercor/bhm174).
- Lohmann, G., von Cramon, D.Y., Steinmetz, H., 1999. Sulcal variability of twins. *Cereb. Cortex* 9, 754–763. doi:[10.1093/cercor/9.7.754](https://doi.org/10.1093/cercor/9.7.754).
- Luders, E., Thompson, P.M., Narr, K.L., Toga, A.W., Jancke, L., Gaser, C., 2006. A curvature-based approach to estimate local gyration on the cortical surface. *Neuroimage* 29, 1224–1230. doi:[10.1016/j.neuroimage.2005.08.049](https://doi.org/10.1016/j.neuroimage.2005.08.049).
- Lyu, I., Seong, J.-K., Shin, S.Y., Im, K., Roh, J.H., Kim, M.-J., Kim, G.H., Kim, J.H., Evans, A.C., Na, D.L., Lee, J.-M., 2010. Spectral-based automatic labeling and refining of human cortical sulcal curves using expert-provided examples. *Neuroimage* 52, 142–157. doi:[10.1016/j.neuroimage.2010.03.076](https://doi.org/10.1016/j.neuroimage.2010.03.076).
- Maclaren, J., Han, Z., Vos, S.B., Fischbein, N., Bammer, R., 2014. Reliability of brain volume measurements: A test-retest dataset. *Sci. Data* 1, 140037. doi:[10.1038/sdata.2014.37](https://doi.org/10.1038/sdata.2014.37).
- Meng, Y., Li, G., Lin, W., Gilmore, J.H., Shen, D., 2014. Spatial distribution and longitudinal development of deep cortical sulcal landmarks in infants. *Neuroimage* 100, 206–218. doi:[10.1016/j.neuroimage.2014.06.004](https://doi.org/10.1016/j.neuroimage.2014.06.004).
- Miles, J.H., 2011. Autism spectrum disorders—a genetics review. *Genet. Med.* 13, 278–294. doi:[10.1097/GIM.0b013e3181ff67ba](https://doi.org/10.1097/GIM.0b013e3181ff67ba).
- Narr, K.L., Bilder, R.M., Kim, S., Thompson, P.M., Szeszko, P., Robinson, D., Luders, E., Toga, A.W., 2004. Abnormal gyral complexity in first-onset schizophrenia. *Biol. Psychiatry* 55, 859–867. doi:[10.1016/j.biopsych.2003.12.027](https://doi.org/10.1016/j.biopsych.2003.12.027).
- Nie, J., Guo, L., Li, G., Faraco, C., Stephen Miller, L., Liu, T., 2010. A computational model of cerebral cortex folding. *J. Theor. Biol.* 264, 467–478. doi:[10.1016/j.jtbi.2010.02.002](https://doi.org/10.1016/j.jtbi.2010.02.002).
- Nie, J., Guo, L., Li, K., Wang, Y., Chen, G., Li, L., Chen, H., Deng, F., Jiang, X., Zhang, T., Huang, L., Faraco, C., Zhang, D., Guo, C., Yap, P.-T., Hu, X.X., Li, G., Lv, J., Yuan, Y., Zhu, D., Han, J., Sabatinelli, D., Zhao, Q., Miller, L.S., Xu, B., Shen, P., Platt, S., Shen, D., Liu, T., 2012. Axonal fiber terminations concentrate on gyri. *Cereb. Cortex* 22, 2831–2839. doi:[10.1093/cercor/bhr361](https://doi.org/10.1093/cercor/bhr361).
- Nordahl, C.W., Dierker, D., Mostafavi, I., Schumann, C.M., Rivera, S.M., Amaral, D.G., Van Essen, D.C., 2007. Cortical folding abnormalities in autism revealed by surface-based morphometry. *J. Neurosci.* 27.
- Perrot, M., Rivière, D., Mangin, J.-F., 2011. Cortical sulci recognition and spatial normalization. *Med. Image Anal.* 15, 529–550. doi:[10.1016/j.media.2011.02.008](https://doi.org/10.1016/j.media.2011.02.008).
- Philip, R.C.M., Dauvermann, M.R., Whalley, H.C., Baynam, K., Lawrie, S.M., Stanfield, A.C., 2012. A systematic review and meta-analysis of the fMRI investigation of autism spectrum disorders. *Neurosci. Biobehav. Rev.* 36, 901–942. doi:[10.1016/j.neubiorev.2011.10.008](https://doi.org/10.1016/j.neubiorev.2011.10.008).
- Rash, B.G., Tomasi, S., Lim, H.D., Suh, C.Y., Vaccarino, F.M., 2013. Cortical gyration induced by fibroblast growth factor 2 in the mouse brain. *J. Neurosci.* 33, 10802–10814. doi:[10.1523/JNEUROSCI.3621-12.2013](https://doi.org/10.1523/JNEUROSCI.3621-12.2013).
- Ronan, L., Voets, N., Rua, C., Alexander-Bloch, A., Hough, M., Mackay, C., Crow, T.J., James, A., Giedd, J.N., Fletcher, P.C., 2013. Differential tangential expansion as a mechanism for cortical gyration. *Cereb. cortex* doi:[10.1093/cercor/bht082](https://doi.org/10.1093/cercor/bht082).
- Schaer, M., Cuadra, M.B., Tamarit, L., Lazeyras, F., Eliez, S., Thiran, J.-P., 2008. A surface-based approach to quantify local cortical gyration. *IEEE Trans. Med. Imaging* 27, 161–170. doi:[10.1109/TMI.2007.903576](https://doi.org/10.1109/TMI.2007.903576).
- Seong, J.-K., Im, K., Yoo, S.W., Seo, S.W., Na, D.L., Lee, J.-M., 2010. Automatic extraction of sulcal lines on cortical surfaces based on anisotropic geodesic distance. *Neuroimage* 49, 293–302. doi:[10.1016/j.neuroimage.2009.08.013](https://doi.org/10.1016/j.neuroimage.2009.08.013).
- Shi, Y., Thompson, P.M., Dinov, I., Toga, A.W., 2008. Hamilton-Jacobi skeleton on cortical surfaces. *IEEE Trans. Med. Imaging* 27, 664–673. doi:[10.1109/TMI.2007.913279](https://doi.org/10.1109/TMI.2007.913279).
- Stigler, K.A., McDonald, B.C., Anand, A., Saykin, A.J., McDougle, C.J., 2011. Structural and functional magnetic resonance imaging of autism spectrum disorders. *Brain Res* 1380, 146–161. doi:[10.1016/j.brainres.2010.11.076](https://doi.org/10.1016/j.brainres.2010.11.076).
- Tao, X., Han, X., Rettmann, M.E., Prince, J.L., Davatzikos, C., 2001. Statistical Study on Cortical Sulci of Human Brains. Springer, Berlin Heidelberg, pp. 475–487. doi:[10.1007/3-540-45729-1_51](https://doi.org/10.1007/3-540-45729-1_51).
- Toro, R., Perron, M., Pike, B., Richer, L., Veillette, S., Pausova, Z., Paus, T., 2008. Brain size and folding of the human cerebral cortex. *Cereb. Cortex* 18, 2352–2357. doi:[10.1093/cercor/bhm261](https://doi.org/10.1093/cercor/bhm261).
- Van Essen, D.C., 1997. A tension-based theory of morphogenesis and compact wiring in the central nervous system. *Nature* 385, 313–318. doi:[10.1038/385313a0](https://doi.org/10.1038/385313a0).
- Wallace, G.L., Robustelli, B., Dankner, N., Kenworthy, L., Giedd, J.N., Martin, A., 2013. Increased gyration, but comparable surface area in adolescents with autism spectrum disorders. *Brain* 136.
- Xiao, H., Peng, H., 2013. APP2: automatic tracing of 3D neuron morphology based on hierarchical pruning of a gray-weighted image distance-tree. *Bioinformatics* 29, 1448–1454. doi:[10.1093/bioinformatics/btt170](https://doi.org/10.1093/bioinformatics/btt170).
- Xu, G., Knutson, A.K., Dikranian, K., Kroenke, C.D., Bayly, P.V., Taber, L.A., 2010. Axons pull on the brain, but tension does not drive cortical folding. *J. Biomech. Eng.* 132, 71013. doi:[10.1115/1.4001683](https://doi.org/10.1115/1.4001683).
- Yeo, B.T.T., Yu, P., Grant, P.E., Fischl, B., Golland, P., 2008. Shape analysis with over-complete spherical wavelets. *MICCAI, LNCS, Lecture Notes in Computer Science* 5241, 468–476. doi:[10.1007/978-3-540-85988-8](https://doi.org/10.1007/978-3-540-85988-8).
- Shi, Y., Tu, Z., Reiss, A.L., Dutton, R.A., Lee, A.D., Galaburda, A.M., Dinov, I., Thompson, P.M., Toga, A.W., 2009. Joint sulcal detection on cortical surfaces with graphical models and boosted priors. *IEEE Trans. Med. Imaging* 28, 361–373. doi:[10.1109/TMI.2008.2004402](https://doi.org/10.1109/TMI.2008.2004402).
- Zhang, T., Chen, H., Guo, L., Li, K., Li, L., Zhang, S., Shen, D., Hu, X., Liu, T., 2014. Characterization of U-shape streamline fibers: methods and applications. *Med. Image Anal.* doi:[10.1016/j.media.2014.04.005](https://doi.org/10.1016/j.media.2014.04.005).
- Zhang, T., Razavi, M.J., Li, X., Chen, H., Liu, T., Wang, X., 2016. Mechanism of consistent gyrus formation: an experimental and computational study. *Sci. Rep.* 6, 37272.
- Zilles, K., Armstrong, E., Schleicher, A., Kretschmann, H.-J., 1988. The human pattern of gyration in the cerebral cortex. *Anat. Embryol. (Berl.)* 179, 173–179. doi:[10.1007/BF00304699](https://doi.org/10.1007/BF00304699).